



Geometric and electronic effects of bimetallic Ni–Re catalysts for selective deoxygenation of m-cresol to toluene



Feifei Yang^a, Dan Liu^a, Hua Wang^a, Xiao Liu^a, Jinyu Han^a, Qingfeng Ge^{a,b,*}, Xinli Zhu^{a,*}

^a Collaborative Innovation Center of Chemical Science and Engineering, School of Chemical Engineering and Technology, Tianjin University, Tianjin 300072, China

^b Department of Chemistry and Biochemistry, Southern Illinois University, Carbondale, IL 62901, United States

ARTICLE INFO

Article history:

Received 17 October 2016

Revised 21 December 2016

Accepted 4 January 2017

Keywords:

Ni–Re/SiO₂

Bimetallic catalyst

m-Cresol

Hydrodeoxygenation

Deoxygenation

Hydrogenation

C–C hydrogenolysis

ABSTRACT

Ni–Re/SiO₂ bimetallic catalysts were prepared using a co-impregnation method and tested in vapor phase hydrodeoxygenation of m-cresol at 300 °C and 1 atm H₂. In contrast to the use of unselective monometallic Ni/SiO₂ for catalyzing deoxygenation, hydrogenation, and C–C hydrogenolysis reactions, bimetallic 5% Ni–2.5%Re/SiO₂ improved the intrinsic reaction rate of the hydrodeoxygenation reaction by a factor of 6, with the turnover frequency for selective deoxygenation to toluene increased by four times, while that for C–C hydrogenolysis to methane was reduced by one-half. Characterization results from X-ray diffraction, Raman, transmission electron microscopy, X-ray photoelectron spectroscopy, infrared spectroscopy of CO adsorption, H₂ temperature-programmed reduction, and CO chemisorption indicate that adding Re increased Ni dispersion and resulted in Ni–Re surface alloy formation after reduction. The presence of Re in the surface alloy breaks the continuous Ni surface into smaller ensembles (geometric effect) and reduces the *d*-band electron density of Ni (electronic effect). Results from density functional theory calculations indicate that the Ni–Re neighboring site is the active site for breaking the C–O bond by adsorbing the O atom on Re and the phenyl ring on the neighboring Ni atoms, which facilitates deoxygenation to toluene. The reduced Ni ensemble size inhibits the hydrogenolysis of the C–C bond by destabilizing the transition state, whereas the reduction of the electronic density in *d* states of Ni weakens the adsorption of the phenyl ring, and both contribute to the greatly reduced methane production from successive C–C hydrogenolysis.

© 2017 Elsevier Inc. All rights reserved.

1. Introduction

The lignin fraction of lignocellulosic biomass has relatively low oxygen content in comparison to cellulose and hemicellulose [1,2]. Depolymerization (for example, fast pyrolysis) of lignin results in phenolic compounds, such as phenol, cresol, anisole, guaiacol, and syringol [3]. These are important building blocks for fuels and chemicals after complete or partial removal of the oxygen content. Catalytic hydrodeoxygenation (HDO) is a key step in oxygen removal [2].

Many studies on HDO of phenolics have been performed using various catalysts, including hydrodesulfurization (HDS) catalysts (CoMoS and NiMoS) [4,5], hydrogenating catalysts (Ni and Pt) [6,7], zeolites [8], metal oxides [9], and metal phosphides [10], and operated under very different conditions to achieve a high degree of oxygen removal and to explore the reaction mechanism. During HDO of phenolics, a number of reactions, such as hydro-

genation of the phenyl ring, deoxygenation, C–C hydrogenolysis, and transalkylation, may take place at the same time, depending on the catalysts and operating conditions. These reactions, occurring in an uncontrolled manner, lead to a mixture of products with high hydrogen consumption and low liquid products yield. Recently, more attention has been paid to selective deoxygenation of phenolics to aromatics with reduced hydrogen consumption under mild conditions (low pressure and intermediate temperature) [11]. These mild conditions are suitable for processing phenolics produced from fast pyrolysis before their condensation to unstable liquids at low temperatures. Reducible metal oxides, such as FeO_x and MoO_x, appear to be highly selective for deoxygenation of phenolics to aromatics at relatively high temperatures [9,12]. On the other hand, typical hydrogenating catalysts, such as Pt, Pd, Ni, and Ru, are more active and could be operated at lower temperatures. However, they tend to hydrogenate the phenyl ring rather than to deoxygenate it [6,7,13–15]. In addition, Ni and Ru have been reported to be highly active for catalyzing C–C hydrogenolysis to form low-value short-chain hydrocarbons [6,13,14]. Combining a hydrogenating metal and an oxophilic metal (reducible metal

* Corresponding authors.

E-mail addresses: qge@chem.siu.edu (Q. Ge), xinlizhu@tju.edu.cn (X. Zhu).

oxide) forms a bimetallic catalyst, such as Ni–Co [16], Pt–Mo [17], Pt–Co [18], Pt–Zn [19], Pd–Fe [20], or Ni–Fe [21]. These bimetallic catalysts are expected to balance the activity and selectivity of deoxygenation and hydrogenation, and have been explored for HDO of phenolics. For example, Nie and Resasco reported that the Ni–Fe catalyst is selective for deoxygenation of *m*-cresol to toluene, and proposed that Fe helped the hydrogenation of the tautomerization intermediate from *m*-cresol to 3-methyl-3,5-cyclohexadienol, which is then quickly dehydrated to toluene [21]. It is noted that the Ni–Fe catalyst is less active than the Ni catalyst. Sun et al. reported deoxygenation of guaiacol and *m*-cresol to aromatics over a Pd–Fe catalyst and suggested that Fe is the active site for direct deoxygenation, whereas Pd is the active site for activating hydrogen [20,22]. The addition of 5% Pd improves the activity of Fe₂O₃ by a factor of 2 [22]. Clearly, more active and selective catalysts for conversion of phenolics to aromatics are desirable. Although catalysts based on bimetallics show promise in improving the selectivity, the nature of the active site and the mechanism for selective deoxygenation are not yet clear.

In this work, we report a highly active bimetallic Ni–Re/SiO₂ catalyst for selective deoxygenation of *m*-cresol to toluene that greatly inhibits C–C hydrogenolysis under mild conditions. *m*-Cresol was used as a model compound because it is an important intermediate product from HDO of complex phenolic compounds, such as guaiacol [23,24]. The inert silica was used to avoid complications due to the support, and therefore, to allow us to focus on better understanding the role of the bimetallic catalysts. Using a combination of detailed characterizations and density functional theoretical calculation, the active site for deoxygenation is determined to be the Ni–Re neighboring sites.

2. Experimental

2.1. Catalyst preparation

The bimetallic Ni–Re catalysts were prepared using incipient wetness co-impregnation of SiO₂ (Sigma, $S_{\text{BET}} = 200 \text{ m}^2/\text{g}$) with aqueous solutions of calculated amounts of Ni(NO₃)₂·6H₂O (Strem Chemicals) and NH₄ReO₄ (Alfa). After impregnation for 12 h, the samples were dried overnight at 120 °C, followed by calcination at 400 °C for 4 h with a heating rate of 2 °C/min. The amount of Ni loading was 5 wt.%, while Re loading was varied from 0 to 10 wt.%. The catalyst was denoted as 5Ni_XRe, where 5 and X represent the weight percentages of Ni and Re, respectively, in the sample. The catalyst powder was pressed, crushed, and sieved to 40–60 mesh for reaction.

2.2. Catalyst characterization

Nitrogen adsorption was recorded at liquid nitrogen temperature in an automatic Micrometrics Digisorb 2600 analyzer. The catalysts were outgassed at 350 °C prior to measurements. The specific surface area of the catalysts was calculated using the Brunauer–Emmett–Teller (BET) method in the relative pressure range $0.005 < p/p_0 < 0.27$.

X-ray diffraction (XRD) patterns of the catalyst samples were recorded on a Rigaku D/max 2500 diffractometer with a Cu K α radiation source ($\lambda = 1.54056 \text{ \AA}$) in the 2θ range 20°–80°.

The Raman spectra were obtained on a Renishaw Raman spectrometer, with an Ar⁺ ion laser (532 nm) being the exciting light source. The focusing spot size was about 1 μm . All spectra were collected at room temperature, with an acquisition time of 10 s/scan and a resolution of 2 cm^{-1} .

Hydrogen temperature-programmed reduction (H₂ TPR) was performed on a Chemisorb 2750 (Micrometrics). Prior to measure-

ment, a catalyst sample of 40 mg was loaded in a U-tube quartz reactor and pretreated with flowing N₂ at 300 °C for 1 h. After the sample was cooled to room temperature, the gas was shifted to 5% H₂/Ar (25 mL/min). After the signal was stabilized, the sample was heated linearly to 800 °C at a rate of 10 °C/min. The amount of hydrogen uptake was monitored on line by a thermal conductive detector.

The transmission electron microscopy (TEM) images were obtained on a JEM 2010F field emission system operated at 200 kV. The fine catalyst powder was dispersed ultrasonically in ethanol for 30 min and a drop of the suspension was deposited on a carbon-coated copper grid for TEM measurement.

X-ray photoelectron spectroscopy (XPS) was performed on a PHI 1600 ESCA spectrometer equipped with an AlK α X-ray radiation source ($h\nu = 1486.6 \text{ eV}$). Catalyst samples were prereduced at 450 °C for 1 h *ex situ* before each measurement. The binding energy (BE) values were referenced to the C1s peak at 284.5 eV.

Fourier transform infrared spectra (FTIR) of CO adsorption were recorded on a Nicolet 6700 (Thermo Scientific), equipped with a liquid-N₂-cooled mercury–cadmium–tellurium detector and a transmittance cell. The catalyst wafer (20 mg) was reduced *in situ* at 450 °C for 1 h with flowing H₂ at 30 mL/min. After that, the sample was cooled to room temperature in flowing He at 30 mL/min and then the background was recorded. The sample was exposed to 5% CO/He (30 mL/min) for 30 min, followed by He purging for another 30 min. The spectra were recorded at a resolution of 4 cm^{-1} and 128 scans.

The dispersion of Ni was estimated based on dynamic CO chemisorption, measured in a microreactor system equipped with a Cirrus 200 mass spectrometer (MKS). The system consisted of an oven with a temperature controller, gas delivery system, micro quartz reactor (6 mm o.d.), and six-port valve. Catalyst samples (50 mg, 40–60 mesh) were reduced at 450 °C for 1 h in flowing H₂, followed by He purging (30 mL/min) for another 30 min. Then the temperature was decreased to room temperature. Pulses of 5% CO/He (100 μL) were sent to the catalyst through the six-port valve until a constant CO peak area was reached.

NH₃ and isopropylamine temperature-programmed desorption (NH₃ TPD and IPA TPD) were measured on the same system as CO chemisorption. A catalyst sample of 100 mg was reduced at 450 °C for 1 h and then purged with flowing He (30 mL/min) for another 30 min. The temperature was reduced to 100 °C. For NH₃ TPD, the sample was exposed to a stream of 2% NH₃/He (30 mL/min) for 30 min. For IPA TPD, liquid IPA (5 μL /pulse, 10 pulse, 3 min/pulse) was injected using a microsyringe manually and vaporized before entering the reactor. After the sample was flushed with flowing He (30 mL/min) for 30 min, the temperature was increased to 650 °C at a rate of 10 °C/min. The quantification was done by injecting pulses of 2% NH₃/He (10 mL/pulse).

Diffuse reflectance infrared Fourier transform spectroscopy (DRIFTS) of pyridine adsorption were measured using a Frontier spectrometer (PerkinElmer), equipped with a diffuse reflectance accessory and a reaction chamber (Harrick). A fine powder catalyst was loaded into the sample cup of the chamber. After the sample was reduced at 450 °C for 1 h and purged with He for 30 min, it was cooled to 100 °C, at which a background spectrum was recorded. Pyridine vapor was then introduced for 30 min, followed by purging using He for another 30 min. The DRIFT spectra were recorded at a resolution of 4 cm^{-1} with 64 scans.

2.3. Density functional theory calculations of phenol adsorption

Density functional theory (DFT) periodic slab calculations were carried out using the Vienna Ab Initio Simulation Package (VASP) [25–27]. The periodic DFT code uses the projector-augmented wave (PAW) method to describe the effective core potentials and

plane waves for the valence electrons [27,28]. The exchange-correlation energy of interacting electrons was evaluated using the Perdew–Burke–Ernzerhof (PBE) functional [29].

Bare Ni and Re-doped Ni (1 1 1) (referred to as (Re)Ni(1 1 1) in the following discussion) surfaces were modeled with a four-layer slab in a p (4×4) surface unit cell, separated by at least 14 Å of vacuum in the z -direction. The computed bulk lattice constant of 3.519 Å for Ni was used to construct the slabs for surface calculations. The atoms in the bottom two layers were fixed, while those in the top two layers were allowed to relax. A cutoff energy of 400 eV and a ($2 \times 2 \times 1$) k -point grid were found to provide converged adsorption energies [30]. The atomic structures were relaxed using either the quasi-Newton scheme or the conjugate gradient algorithm as implemented in the VASP code.

The adsorption energy was defined as

$$E_{\text{ads}} = E_{(\text{adsorbate/surface})} - E_{(\text{adsorbate})} - E_{(\text{bare surface})} \quad (1)$$

where $E_{(\text{adsorbate/surface})}$ is the total energy of an adsorbate bound to Ni or the Ni–Re slab, $E_{(\text{adsorbate})}$ is the total energy of a molecule in gas phase, and $E_{(\text{bare surface})}$ is the total energy of the bare slab. Phenol was used as a model compound. The transition state for deoxygenation was confirmed to have only one imaginary mode in normal mode frequency analysis.

2.4. Catalytic activity

The vapor-phase conversion of *m*-cresol over the Ni, Ni–Re, and Re catalysts was evaluated in a downflow fixed-bed quartz tube reactor (6 mm o.d.) under atmospheric pressure, as has been reported [13,31]. Briefly, the catalyst sample (40–60 mesh) was placed between two layers of quartz wool in the middle of the reactor. The catalyst was reduced at 450 °C for 1 h in flowing H_2 (30 ml/min) and then cooled down to reaction temperature. *m*-Cresol was fed using a syringe pump (KDS100, kd scientific) and vaporized before entering the reactor. H_2 /*m*-cresol molar ratio was kept at 60 in all runs. The products were quantified on line in a gas chromatograph (GC7890B, Agilent). The effluent was trapped by methanol in an ice water bath, and its components were identified using GC-MS (Shimadzu QP2010SE). Fresh samples were used for each space time ($W/F, g_{\text{cat}}g_{\text{reactant}}^{-1} \text{ h}$). The conversion and yield are reported in $\text{mol}_{\text{carbon}}\%$.

3. Results and discussion

3.1. Catalyst characterizations

3.1.1. BET and XRD

As shown in Table 1, the specific surface area of the catalysts decreased moderately as the amount of Re increased.

Table 1
Physical properties of monometallic 5Ni, 2.5Re, and bimetallic Ni–Re catalysts.

Catalyst	Ni/Re		S_{BET} (m^2/g)	Particle size (nm)			Lattice distance (nm)		Crystal structure	Lattice constant (Å)		CO/Ni	Acid density ^c ($\mu\text{mol}/\text{g}$)
	Mass	Mole		XRD ^a	XRD ^b	TEM ^b	XRD	TEM		a or b	c		
5Ni	–	–	181	22.9	21.3	25.5	0.204	0.204	fcc	3.530	3.530	0.016	15.3
5Ni1Re	5	15.9	184	13.6	8.0	–	0.205	–	fcc	3.551	3.551	0.04	15.4
5Ni2.5Re	2	6.35	182	11.5	7.5	9.9	0.206	0.207	fcc	3.565	3.565	0.045	25.1
5Ni5Re	1	3.17	167	3.4	2.3	–	0.209	–	hcp	2.744	4.441	0.085	51.2
5Ni10Re	0.5	1.59	145	3.0	3.0	–	0.210	–	hcp	2.759	4.451	0.103	60.5
2.5Re	–	–	197	–	4.9	5.5	0.212	–	hcp	2.764	4.482	n.d. ^d	20.7

^a Particle size of calcined catalysts.

^b Particle size of reduced catalysts.

^c Derived from NH_3 TPD.

^d Not detected.

The XRD patterns of Ni–Re catalysts before and after reduction are shown in Fig. 1, with the particle sizes estimated using the Scherrer equation reported in Table 1. For the fresh catalysts (Fig. 1A), sharp diffraction peaks attributed to NiO were observed for the monometallic 5Ni sample. Increasing the amount of Re resulted in diffraction peaks of NiO broadening and weakening gradually. Therefore, the estimated particle size of NiO decreased as the amount of Re increased (Table 1). However, no diffraction peaks attributable to ReO_x were observed in either the monometallic 2.5Re sample or bimetallic Ni–Re samples, regardless of the Re loadings. These results indicate that ReO_x species were highly dispersed in all bimetallic Ni–Re samples and were probably in proximity to NiO, which, in turn, increases the dispersion of NiO on silica as compared with that for the monometallic Ni samples.

When the catalysts were reduced at 450 °C for 1 h (Fig. 1B), metallic Ni of face-centered cubic (fcc) structure and metallic Re of hexagonal closed packed (hcp) structure were clearly observable for the monometallic 5Ni and 2.5Re catalysts, respectively. The presence of Re in bimetallic catalysts led to the broadening of the Ni diffraction peaks, indicating that the size of Ni or bimetallic Ni–Re particles was reduced, in good agreement with the Ni–Re/ZrO₂ catalyst [32]. Interestingly, the diffraction peak of Ni(1 1 1) at 2θ of 44.41° for monometallic 5Ni shifted gradually to a lower value of 43.95° for bimetallic 5Ni2.5Re. This shift resulted from the lattice expansion of the Ni unit cell (Table 1), likely due to Re (which has a larger atomic diameter than Ni) penetrating into the Ni lattice during the reduction. This phenomenon has been considered as an indication of alloy formation in the bimetallic Ni–Re catalyst [33] and other bimetallic catalysts, such as Ni–Fe [34] and Ni–Co [16]. When the Re loading was increased to >2.5%, the diffraction peaks shifted further to lower values and the shape of the patterns changed from fcc Ni to hcp Re, which might indicate that the structure of bimetallic particles changed from fcc to hcp as a result of increased Re content. It is worth noting that the estimated particle size for the Ni–Re samples after reduction (Table 1) reflects contributions from both Ni and Re as Re penetrated into the Ni lattice during the reduction, particularly at high Re loadings. The particle size of 5Ni10Re is slightly greater than that of 5Ni5Re as a result of the doubled Re loading.

3.1.2. Raman spectroscopy

Raman spectroscopy was used to probe the surface structure of ReO_x species in Ni–Re catalysts. As shown in Fig. 2, 5Ni and bare SiO₂ showed similar feature with bands at 603 and 489 cm^{-1} and a broad band at $\sim 400 \text{ cm}^{-1}$, which are characteristic bands of silica supports [35]. The Ni–O stretching band at 550–500 cm^{-1} is very weak [36] and may be masked by the bands of silica. In contrast, the 5Re sample showed sharp and strong bands at 965, 914, 891, and 345 cm^{-1} . These bands can be assigned to $\nu_s(\text{Re}=\text{O})$, $\nu_{\text{as}}(-$

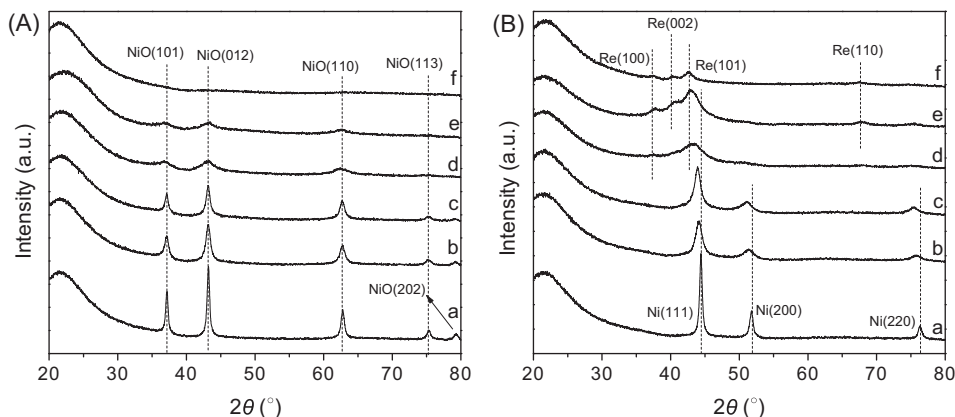


Fig. 1. XRD patterns of monometallic 5Ni, 2.5Re, and bimetallic Ni–Re catalysts: (A) fresh catalysts; (B) reduced at 450 °C for 1 h. (a) 5Ni; (b) 5Ni1Re; (c) 5Ni2.5Re; (d) 5Ni5Re; (e) 5Ni10Re; (f) 2.5Re.

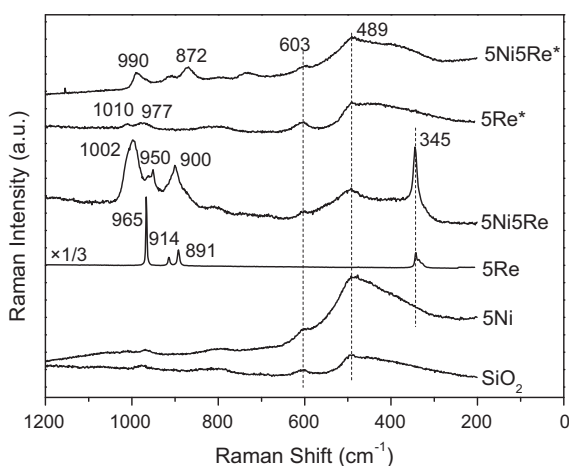


Fig. 2. Raman spectra of different catalysts. An * indicates that the catalysts were reduced ex situ at 450 °C for 1 h; the others were fresh catalysts.

Re=O), $\nu_s(\text{Re}-\text{O}-\text{Si})$, and $\delta(\text{O}-\text{Re}-\text{O})$, respectively, of isolated tetrahedral ReO_4^- species with a structure of $\text{Si}-\text{O}-\text{Re}(=\text{O})_3$ on the silica surface [35,37,38]. No characteristic bands of Re–O–Re at 800, 450, and 200–150 cm^{-1} were observed, suggesting that the ReO_x are in the state of isolated ReO_4^- highly dispersed on the surface instead of polymeric Re_2O_7 [38]. Consequently, XRD patterns of the fresh catalyst did not show any signal of ReO_x . In comparison with monometallic 5Re, the bands of isolated tetrahedral ReO_4^- species in bimetallic 5Ni5Re shifted to higher wavenumbers of 1002, 965, 950, and 900 cm^{-1} , with reduced peak intensity and broadened peak width. By analogy to Ir–Re/SiO₂ catalysts [39], these changes might be a result of the decrement in the bond length of Re=O due to the formation of Ni–O–Re(=O)₃ species on the surfaces of NiO particles. This close proximity between NiO and ReO_x species would prevent the growth of NiO particle during calcination and facilitate the penetration of Re atom into the Ni unit cell during reduction. When the samples were reduced at 450 °C, the band intensities of ReO_x species decreased significantly, indicating that most of the ReO_x species were reduced by the hydrogen treatment.

3.1.3. H₂ TPR

H₂ TPR was conducted to investigate the interaction between NiO and ReO_x (Fig. 3). Monometallic 2.5Re displayed a hydrogen consumption peak at 347 °C, while monometallic 5Ni showed a

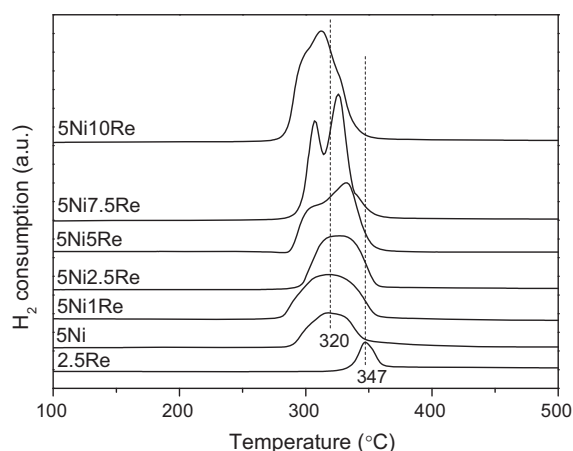


Fig. 3. H₂ TPR profiles of monometallic 5Ni, 2.5Re, and bimetallic Ni–Re catalysts.

broad peak at a slightly lower temperature of 320 °C, indicating that isolated ReO_4^- species with strong interaction with silica are more difficult to reduce than the larger NiO particles with weak interaction with silica. Interestingly, all bimetallic Ni–Re samples showed lower reduction temperatures than monometallic 2.5Re. This is expected, as Ni facilitates the reduction of adjacent ReO_x species through hydrogen activation on Ni and spill over to ReO_x . The lowered reduction temperature indicates that the ReO_x species are in close contact with the NiO particle, consistent with the Raman result. At Re loadings $\leq 5\%$, bimetallic NiRe only showed one reduction peak. When the Re loading was further increased, the reduction peak appears to contain at least two components, which is probably due to the formation of Ni–Re alloys with different Ni/Re ratios.

Quantitative results show that the molar ratio of H₂ consumption to Ni (H₂/Ni) for monometallic 5Ni is 0.95, indicating almost complete reduction of NiO. In contrast, the H₂/Re ratio is 2.4 for monometallic 2.5Re. Similar H₂/Re ratio values of 2.1–2.5 are obtained for bimetallic Ni–Re catalysts, assuming complete reduction of NiO. As indicated in the Raman results, the main ReO_x species is ReO_4^- , in which Re has a formal valence state of +7, requiring a H₂/Re ratio of 3.5 for complete reduction. The difference in measured and theoretical H₂/Re ratios indicates that the Re species were not completely reduced in TPR. Based on the H₂ consumption, we estimated the average valence state of the Re species after the reduction is about +2. Since particles of metallic Re were detected in XRD, we can conclude that the resulting catalyst contains both

completely and partially reduced Re species after reduction treatment. Because Ni helps to reduce ReO_x at lower temperatures, we anticipate that part of the incompletely reduced Re species stay away from the Ni particles due to their strong interaction with the silica support, consistent with the TEM results shown below.

3.1.4. TEM

Representative TEM images of the reduced 5Ni, 5Ni2.5Re, and 2.5Re samples are displayed in Fig. 4. Large nickel particles of ~ 20 nm were observed for monometallic 5Ni (Fig. 4A). In contrast, small and uniform particles of Re with sizes < 5 nm were observed for monometallic 2.5Re (Fig. 4C). These results clearly indicate that Ni tends to aggregate into large particles due to weak interaction with silica, while Re tends to be well dispersed on silica due to the strong oxophilicity of Re, which leads to strong interaction with silica. The presence of Re in the 5Ni2.5Re sample significantly reduced the particle size (Fig. 4B). Although large particles of ~ 20 nm were still present for 5Ni2.5Re, most particles are smaller than 10 nm. In good agreement with the XRD results, the estimated average particle sizes decreased from 25.5 nm for monometallic 5Ni to 9.9 nm for 5Ni2.5Re (Table 1). High-resolution TEM (HR-TEM) measurements were performed to examine the fine structures (see insets in Fig. 4). For 5Ni, the measured lattice fringe is 0.204 nm and agrees well with Ni(111). For 5Ni2.5Re, the lattice fringe is 0.207 nm, which is larger than that of Ni(111) but smaller than that of Re(101) (0.210 nm). In good agreement with the XRD results (Table 1), these results indicate that the penetration of Re atoms into the Ni lattice during reduction resulted in the expansion of lattice, which may be indicative of Ni–Re alloy formation in the bimetallic sample.

The composition of the particles of bimetallic 5Ni2.5Re was further analyzed by high-angle annular dark field scanning transmission electron microscopy (HAADF-STEM), accompanied by energy-dispersive spectroscopy (EDS) analysis. The HAADF-STEM image showed a bimodal distribution of particles with bright larger particles and dark smaller particles (Fig. 5). Single-point EDS analysis of several bright particles showed an Ni/Re ratio ~ 10 (see insets), which is higher than the theoretical ratio of 6.35 for 5Ni2.5Re. This result indicates that the bright larger particle is rich in Ni. Line-scanning EDS analysis (see insets) of a larger particle (along the red line in Fig. 5B) showed that the Ni/Re ratio is higher at the center of the particle, suggesting that Re content decreases from the external surface to the core of the Ni particle due to a longer diffuse path during Re penetration into the Ni particle. EDS mapping conformed that the highly dispersed dark smaller particles (indicated by an arrow in Fig. 5B) on the silica support are rich in Re. As displayed in Fig. 6, the bright larger particles contain Ni and Re uniformly distributed in the particle and are rich in Ni. On the other hand, the small dark particles rich in Re are highly dispersed on the silica support. The STEM results indicate that the Re species in close contact with the Ni species stabilizes the dispersion of Ni on silica.

3.1.5. XPS

The electronic interactions and surface compositions of bimetallic Ni–Re catalysts were analyzed using XPS. Due to the limitations of the instrument, the samples can only be reduced ex situ for XPS measurement. Consequently, the surfaces may have been partially oxidized while being transferred for XPS measurements. To analyze Ni–Re interaction, spectral analysis was performed by fixing the BE of oxidized $\text{Ni}^{2+}2p_{3/2}$ at 856.1 eV and the corresponding shakeup satellite peak at 861.1 eV [40], and oxidized Re^{4+} and Re^{3+} of $4f_{7/2}$ at 42.4 and 40.7 eV, respectively [41]. The results are shown in Fig. 7. In comparison with monometallic 5Ni at 852.7 eV, the BE of $\text{Ni}^{0}2p_{3/2}$ for bimetallic 10Ni5Re shifts to a higher BE by 0.5–853.2 eV (Fig. 7A). On the other hand, the

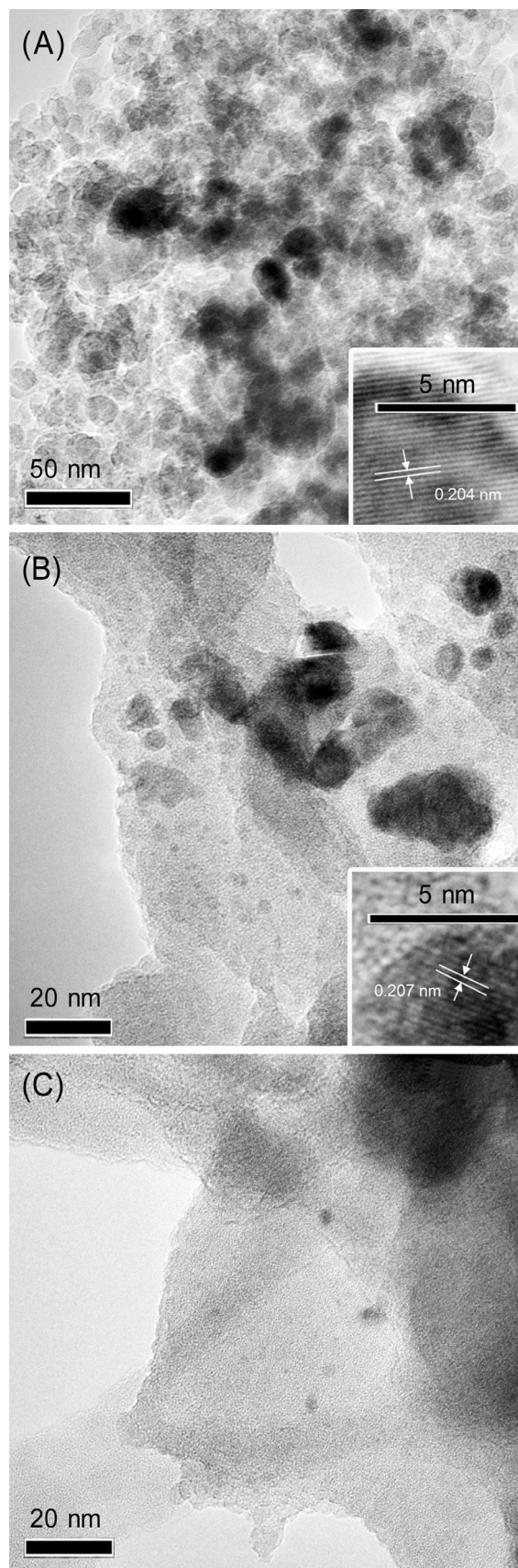


Fig. 4. TEM images of (A) 5Ni; (B) 5Ni2.5Re; (C) 2.5Re. The inserts show the HR-TEM image. The samples were pre-reduced at 450 °C for 1 h.

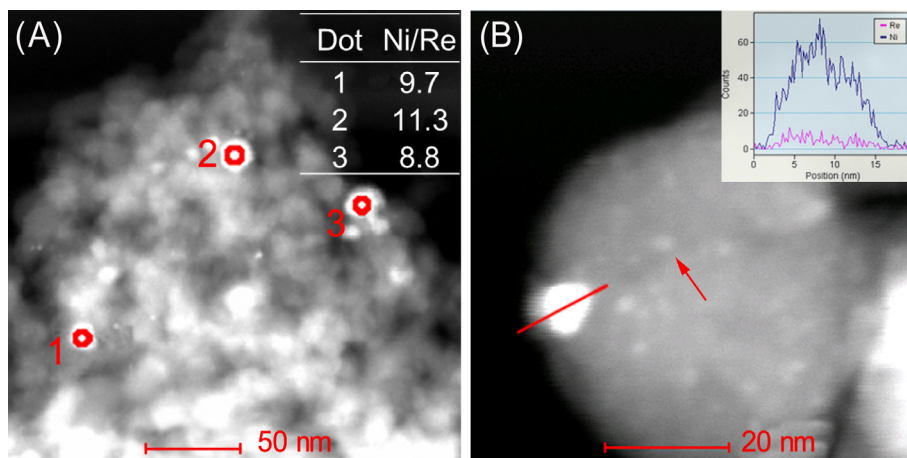


Fig. 5. HAADF-STEM image of 5Ni_{2.5}Re. (A) A larger area with insert shows the Ni/Re molar ratio of several particles; (B) a smaller area with inset shows line scanning results of EDS. The catalyst was prereduced at 450 °C for 1 h.

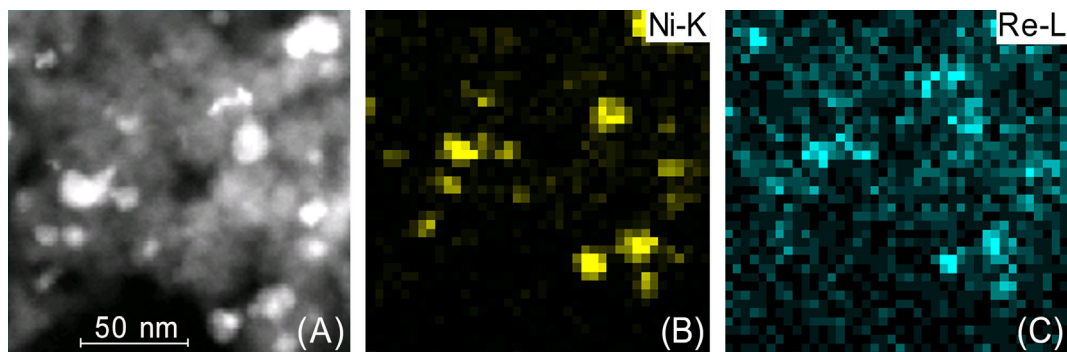


Fig. 6. (A) HAADF-STEM of 5Ni_{2.5}Re revealing the EDS mapping region; (B) EDS mapping of Ni element; (C) EDS mapping of Re element. The catalyst was prereduced at 450 °C for 1 h.

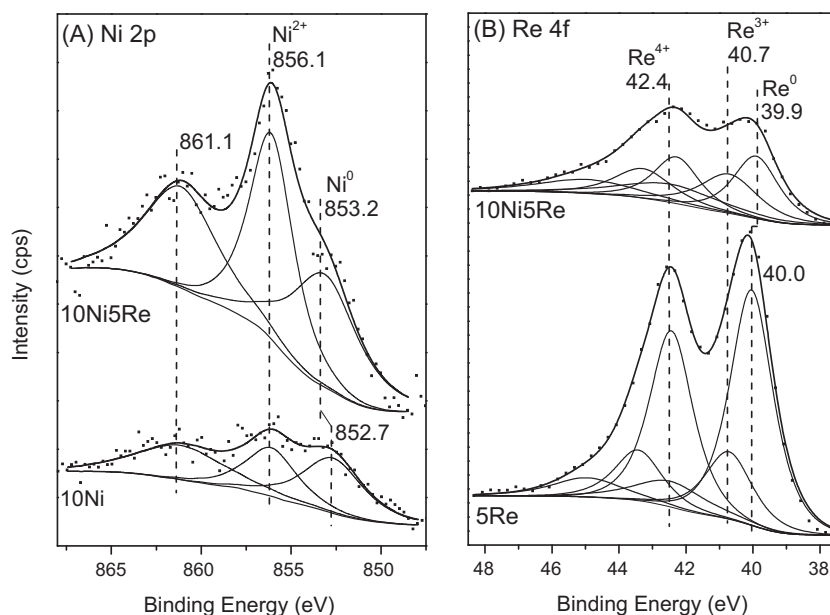


Fig. 7. XPS spectra of (A) Ni_{2p} and (B) Re_{4f}. Dots, experimental data; lines, curve fittings. The samples were prereduced ex situ at 450 °C for 1 h.

BE of Re⁰4_{f_{7/2} only changed slightly, from 40.0 eV for 5Re to 39.9 eV for 10Ni₅Re (Fig. 7B). Consistent with previous work on unsupported Ni–Re [40], the results indicate that the relatively}

electron-rich *d* band of Ni loses its electron density through hybridization either to its 4*s* and 4*p* states or to the relatively

electron-poor d band of Re [42], resulting in the observed shift of the $Ni2p$ state to higher BE.

To further understand the electronic interactions, we analyzed the charge distribution of a Ni–Re dimer. As shown in the isosurfaces of positive and negative charges (Fig. S1 in the Supplementary Material), the Ni end of the Ni–Re dimer concentrated both positive and negative charges, indicating a strong redistribution of electronic charges around the Ni atom. Although the overall charge on Ni is negative, the net reduction of the d electronic density is expected to dominate the observed peak shifts in XPS. In fact, a similar observation has been reported on the Pd–Cu bimetallics, where the overall electron transfer occurred from Cu to Pd but the population of the $Pd4d$ orbitals is lower in the alloy than in the pure metal [43].

As shown in Table 2, the bimetallic 10Ni5Re is more easily oxidized than the monometallics (either 10Ni or 5Ni) after exposure to air. The surface Ni/Si ratio increases significantly from 10Ni to 10Ni5Re, whereas the Re/Si ratio decreases from 5Re to 10Ni5Re, indicating that the Re–Ni interactions in the bimetallic Ni–Re catalyst improve the dispersion of Ni on the surface of SiO_2 . The surface Ni/Re ratio was found to be 3.3, lower than the theoretical value of 6.3. The results indicate a higher dispersion of Re than of Ni, as well as the enrichment of Re on the surface of the bimetallic Ni–Re particles, in good agreement with the EDS line scanning result (Fig. 5B).

3.1.6. FTIR of CO adsorption

Fig. 8 shows IR spectra of CO adsorption on 2.5Re, 5Ni, and 5Ni2.5Re. Two absorption bands at 2036 and 1910 cm^{-1} are present in monometallic 5Ni, which can be ascribed to linear- and bridge-adsorbed CO, respectively [44,45]. The ratio of integrated peak area of linear to bridge adsorption (L/B) is 0.59. This low L/B ratio for 5Ni sample is consistent with the TEM and XRD results, which showed large size of Ni particles. The large Ni particle contains more close-packed Ni(111) facets, which favor bridge over linear adsorption of CO. Interestingly, no CO adsorption band was observed for monometallic 2.5Re. It has been reported that CO only adsorbs on metallic Re but not on ReO_x [46]. Moreover, CO adsorption on metallic Re was reported to be extremely weak at room temperature [47]. Considering the TPR result that Re was not completely reduced during the pretreatment, we can infer that CO barely adsorbed on the Re species in Re-containing samples under this condition.

Compared with CO adsorption on monometallic samples, changes in the important adsorption feature are evident for bimetallic 5Ni2.5Re. In addition to the bands of linear- and bridge-bound CO at 2047 and 1906 cm^{-1} , respectively, a small band at 2090 cm^{-1} and a shoulder band at 2002 cm^{-1} emerged. The former has been assigned to CO linearly adsorbed on defect Ni^0 sites [45]. The latter could not be assigned to CO adsorption on Re^0 due to the absence of characteristic adsorption bands at 2059, 2039, 2016, and 1963 cm^{-1} [48]. Based on the literature [49], we tentatively assign this band to CO linearly adsorbed on Ni^0 (e.g., the Ni atom of the Ni–Re alloy) that is perturbed by vicinal Re, since Re is a strongly oxophilic element. This assignment is sup-

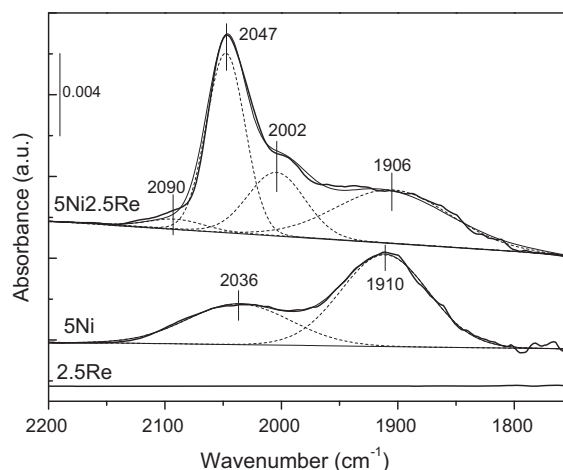


Fig. 8. FTIR spectra of CO adsorption on 5Ni, 2.5Re, and 5Ni2.5Re.

ported by the fact that the band intensity increases with increasing amounts of Re (data not shown). Interestingly, the linear CO band is blue-shifted from 2036 cm^{-1} on 5Ni to 2047 cm^{-1} on bimetallic 5Ni2.5Re. Consistent with the XPS results, this shift could result from electronic interaction between Ni and Re that reduces the d -band electron densities of Ni [40,42,50]. Consequently, the electron back-donation from d orbitals of Ni to the π^* orbital of CO is reduced, and therefore the Ni–C bond is weakened while the C–O bond is strengthened, resulting in a blue shift in the C–O stretching frequency. The most significant change from monometallic 5Ni to bimetallic 5Ni2.5Re is the significantly increased L/B ratio, reaching 1.96 from 0.59. The high L/B ratio indicates that the addition of Re increases the population of terminal sites but reduces the bridge sites for CO adsorption. This is believed to be achieved by breaking the continuity of the Ni surface and forming smaller Ni atom ensembles due to the presence of Re. The reduction of the surface Ni ensembles provided more sites for linear adsorption of CO than for bridge adsorption. We expect that the changes of surface properties also influence the adsorption of phenolics on the surface, and thus the mechanism and selectivity of the HDO reactions.

3.1.7. CO chemisorption

The number of surface active sites was quantified by dynamic pulse chemisorption of CO. The amount of CO adsorbed onto monometallic 2.5Re was under the detection limit of MS, which suggests that Re species do not adsorb CO under this condition, in good agreement with IR results. Since a similar degree of reduction of Re species was achieved over Re-containing samples, the CO adsorbed on bimetallic Ni–Re catalysts is only related to the surface Ni sites. As shown in Table 1, CO/Ni increased significantly with the increasing amount of Re. This result is consistent with the XRD and TEM characterization, suggesting that addition of Re stabilizes the smaller Ni particles through Ni–O–Re interactions

Table 2
Distribution of different valence states of Ni and Re as well as atomic ratios derived from XPS.

Catalyst	Distribution of valence states (%)					Atomic ratio		
	Ni		Re			Ni/Si	Re/Si	Ni/Re
	Ni^0	Ni^{2+}	Re^0	Re^{3+}	Re^{4+}			
10Ni	57.4	42.6	–	–	–	0.027	–	–
5Re	–	–	67.1	21.0	11.9	–	0.072	–
10Ni5Re	45.3	54.7	41.3	33.1	25.7	0.154	0.047	3.3

during calcination and provides more surface Ni sites after reduction.

3.1.8. NH_3 TPD, IPA TPD, and DRIFTS of pyridine adsorption

Since the presence of strong acid sites could affect the reaction pathway and therefore the product distributions [31,51], the acidic property of the bimetallic catalysts has been investigated using NH_3 TPD and IPA TPD. The IPA TPD (data not shown) did not show any Brønsted acid-catalyzed decomposition products of propylene or NH_3 [52,53] for any samples, indicating the absence of strong Brønsted acid sites (BAS) in these samples. This result is consistent with Kawai et al., who performed pyridine TPD on $\text{Re}/\text{Al}_2\text{O}_3$ and showed that a higher reduction temperature changed BAS to Lewis acid sites (LAS) [54]. Fig. 9 shows the NH_3 TPD profiles, with quantified results summarized in Table 1. Again, silica support exhibited no acidity, and both monometallic 5Ni and 2.5Re contain very few acid sites. However, the number of acid sites increases with the increasing Re loading in the bimetallic Ni Re samples. These results suggest that new acid sites are created in the presence of Re upon reduction, in line with previous work, which showed that acid sites could be created in bimetallic catalysts containing a noble hydrogenating metal and an oxophilic metal [55]. It should be noted that the center of the desorption peak is lower than 200 °C in all samples. Taking the IPA TPD results into account, we believe that the acid sites in the bimetallic Ni–Re catalysts are weak LAS. These sites could be the completely and/or partially reduced Re sites adjacent to Ni, which serve as active sites to adsorb the oxygen atom of cresol. Additional DRIFTS measurements of pyridine adsorption were performed (Fig. S2). The adsorption band at 1446 cm^{-1} in both monometallic and bimetallic samples can be assigned to pyridine adsorption on LAS [54]. In contrast, the characteristic adsorption band for pyridine adsorption on BAS at $\sim 1540 \text{ cm}^{-1}$ [54] was absent in all samples, indicating no BAS in presence under this pretreatment condition.

3.2. Phenol adsorption on Ni(111) and (Re)Ni(111)

Based on the characterizations, the Ni(111) surface and the surface with one surface Ni atom replaced by one Re atom were used to represent the monometallic 5Ni and bimetallic Ni–Re catalysts, respectively. The most stable configuration of phenol adsorption on Ni(111) was found to be flat adsorption on a bridge site with an angle between the axis of phenol and the close-packed direction of the (111) surface of 28.2° (configuration Bri28.2), as shown in Fig. 10B. Similarly to phenol adsorption on Pd and Pt surfaces [30], the aromatic ring was adsorbed on the surface through mixed

σ and π bonds of Ni–C, while the O in the –OH group was pushed away from the surface, with a distance of 2.82 Å between O and the nearest Ni atom. The strong repulsion between Ni and O also lifted the connecting carbon atom (C1) away from the aromatic plane by ~ 0.1 Å with respect to other carbon atoms (Table 3). This adsorption configuration is similar to the results of theoretical calculations [56–58] and high-resolution electron energy loss spectroscopy experiments [19,59] on phenol adsorption on Group VIII metals. Compared with phenol adsorption on Ni(111), although flat adsorption was still the most favorable configuration on the (Re)Ni(111) surface, some important features were evident, as shown in Fig. 10C. First, the aromatic ring rotates counterclockwise by 6° on the bridge site (configuration Bri22.1) to place the O atom of phenol on top of the Re atom. Second, the O moves toward Re in the surface due to the strong oxophilicity of Re. The distance between O and Re is 2.41 Å, suggesting the formation of a Re–O bond, which is supported by density of states (DOS) analysis. As shown in Fig. S3, there are obvious overlaps between the d orbitals of Re and the p orbitals of O. Meanwhile, the angle of the O–C1–plane decreases from 30.3° on bare Ni(111) to 22.3° on (Re)Ni(111). Third, in contrast to the H atom of the hydroxyl of phenol pointing to the surface on Ni(111), the H atom is tilted away from the surface on (Re)Ni(111). These structural changes lead to the C–O bond of phenol being lengthened from 1.37 Å in the gas phase and on bare Ni(111) to 1.42 Å on (Re)Ni(111). In addition, the bond length of C1–Ni was reduced by 0.1 Å. In summary, the presence of an oxophilic Re atom in the Ni surface makes the O more easily bound to the surface and the C1 closer to the Ni atom in the surface. Therefore, the C–O bond may cleave more readily on the Ni–Re neighboring sites, resulting in higher HDO reactivity.

We also note that the adsorption of phenol is slightly weaker on (Re)Ni(111) than on bare Ni(111) by 6.8 kJ/mol (Table 3). Recently, McEwen and co-workers showed that flat adsorption of phenol is stronger on Pd(111) than on oxophilic Fe(110), even though there is Fe–O bond but no Pd–O bond formation [60]. Although the aromatic ring is closer to the surface on Fe than on Pd, the charge transfer between Pd and the aromatic ring is more pronounced than that between Fe and the aromatic ring [60], leading to a higher adsorption energy of phenol on Pd(111) than on Fe(110). The XPS results and FTIR results of CO adsorption on bimetallic Ni–Re have shown that the d -band electron density of Ni becomes deficient in the presence of adjacent Re. Thus, one would expect that the deficient Ni d band in Ni–Re reduces the charge transfer between surface Ni and the aromatic ring, and consequently weakens the adsorption strength of phenol on (Re)Ni(111). This weakened adsorption of the aromatic ring facilitates the desorption of aromatic products and prevent the subsequent hydrogenolysis of the C–C bonds.

3.3. Catalytic performance

Fig. 11 compares the major products' evolution as a function of W/F during HDO of *m*-cresol over monometallic 5Ni and bimetallic 5Ni2.5Re catalysts. Apparently, bimetallic 5Ni2.5Re is much more active than monometallic 5Ni. To reach 20% conversion, the required W/F on 5Ni is five times longer than that on 5Ni2.5Re (Fig. 11A). At low conversions, both catalysts showed major products toluene (Tol), 3-methylcyclohexanone (MCHone), 3-methylcyclohexanol (MCHol), phenol (Ph), and methane (CH_4), as a result of three parallel reaction pathways: apparent direct deoxygenation, hydrogenation, and C–C hydrogenolysis (Scheme 1). However, the product distributions are significantly different on the two catalysts. On 5Ni, the hydrogenolysis products (Ph and CH_4) had yields comparable to those of Tol and MCHone. This result is consistent with previous works that showed that nickel catalysts favor multiple C–C hydrogenolysis (ring opening) and

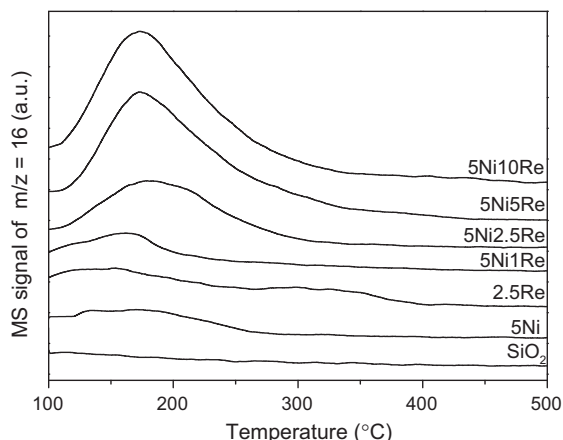


Fig. 9. NH_3 TPD profiles of different catalysts.

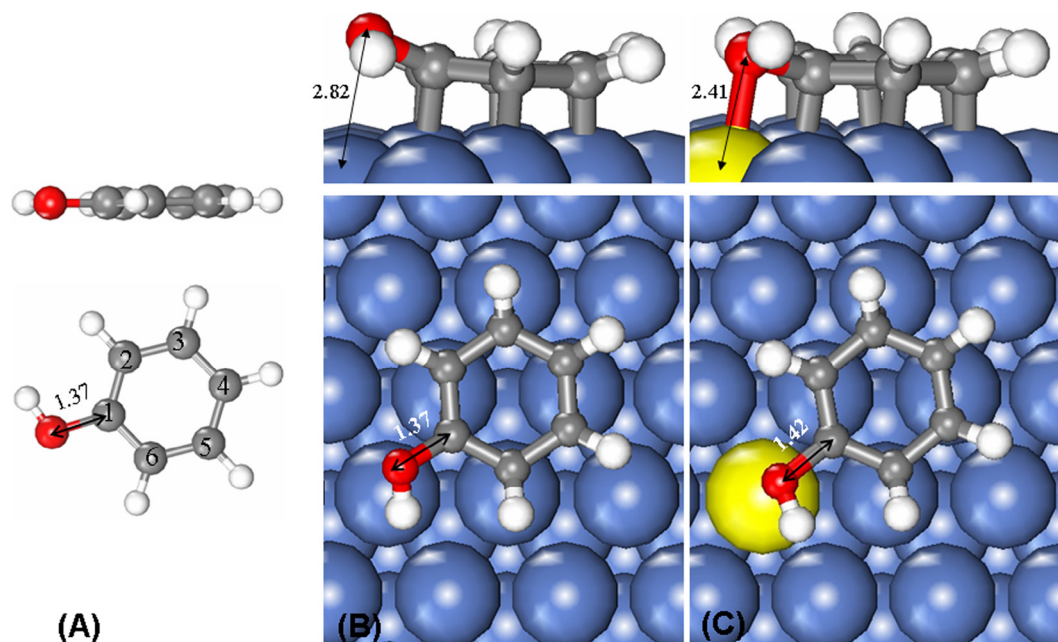


Fig. 10. Structure of (A) gas phase phenol; (B) phenol adsorption onto Ni(111) surface with a structure of Bri28.2; and (C) phenol adsorption onto (Re)Ni(111) surface with a structure of Bri22.1. The unit of the numbers in the figure is Å.

Table 3

The distances of C–Ni, C–O, O–Ni, and O–Re, the angle of the O–C1 plane, and the adsorption energy (E_{ad}) of phenol on Ni(111) and (Re)Ni(111) surfaces.

Surface	Ni(111)	(Re)Ni(111)
C1–Ni (Å)	2.21	2.12
C2–Ni (Å)	2.07	2.03
C3–Ni (Å)	2.06	2.06
C4–Ni (Å)	2.07	2.12
C5–Ni (Å)	2.05	2.03
C6–Ni (Å)	2.03	2.04
C–O (Å)	1.37	1.42
O–Ni (Å)	2.82	–
O–Re (Å)	–	2.41
\angle O–C1–plane ($^{\circ}$)	30.09	22.33
E_{ad} (kJ/mol)	–116.7	–109.9

successive hydrogenolysis at the terminal C–C bond [6,13], resulting in the formation of low-value CH_4 with very high hydrogen consumption. On 5Ni2.5Re, Tol is the dominant product, with CH_4 and Ph being significantly reduced and becoming minor products, while the yields of MCHone and MCHol are slightly reduced. Evidently, selective deoxygenation of m-cresol to Tol is achieved on the bimetallic NiRe catalysts while C–C hydrogenolysis is greatly suppressed.

As shown in Table 4, the minor products include the products from acid-catalyzed primary reactions of isomerization and transalkylation (p- and o-cresol, xylenols, and phenol) and secondary hydrogenation, deoxygenation, and C–C hydrogenolysis products (cyclohexanone, cyclohexanol, benzene, cyclohexane, methylcyclohexane, C_2 – C_6 hydrocarbons). Since the acid strength of bimetallic NiRe is weak (see Fig. 9), acid-catalyzed reactions occur to a limited extent. Furthermore, in contrast to the strong

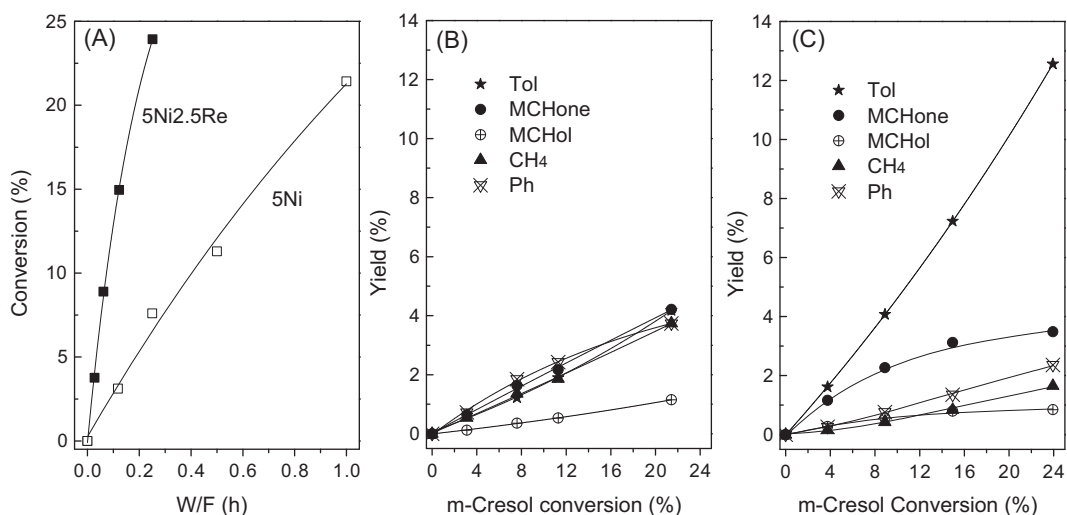
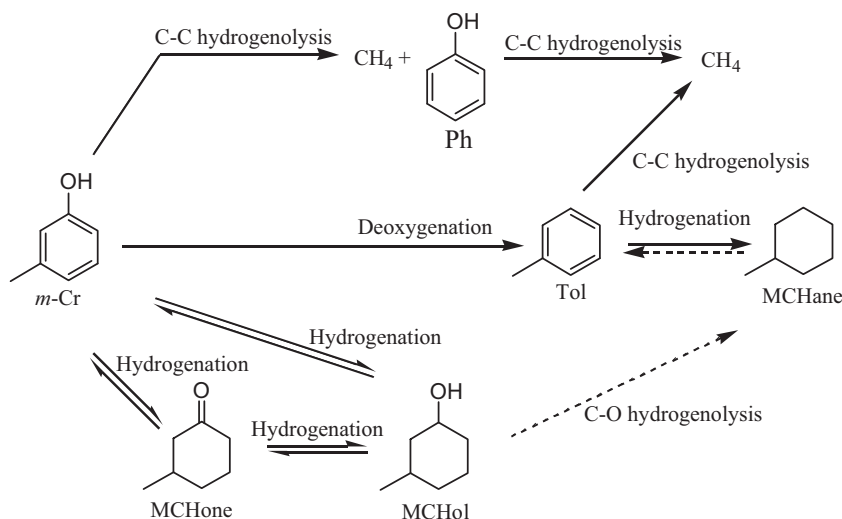


Fig. 11. Effect of W/F on m-cresol conversion over 5Ni and 5Ni2.5Re (A) and major products distribution as a function of m-cresol conversion on 5Ni (B) and 5Ni2.5Re (C). Reaction conditions: $T = 300\text{ }^{\circ}\text{C}$, $P = 1\text{ atm}$, $\text{H}_2/\text{m-cresol} = 60$, TOS = 30 min.



Scheme 1. Major reaction pathway of m-cresol conversion on Ni and Ni–Re catalysts.

Table 4
Effect of catalyst on m-cresol conversion and products distribution.

Catalyst	5Ni	2.5Re	2.5ReO _x ^a	5Ni2.5Re	5Ni+2.5Re ^b
Conversion (%)	10.3	3.0	0.8	47.6	14.9
<i>Product yield (%)</i>					
Tol	1.9	2.9	0.5	23.7	5.8
MCHone	2.2	0	0	3.0	2.4
MCHol	0.5	0	0	0.7	0.4
CH ₄	1.9	0	0	5.6	1.5
Ph	2.4	0	0	5.9	2.3
Ben	0.1	0	0	2.6	0.3
MCHane	0.0	0	0	0.04	0.03
C ₂₋₆	0.2	0	0	0.14	0.09
Xylenols	0.7	0	0	0.9	0.6
Others ^c	0.4	0.1	0.3	5.0	1.5

Note: Reaction conditions: $T = 300\text{ }^{\circ}\text{C}$, $P = 1\text{ atm}$, $\text{H}_2/\text{m-cresol} = 60$, $W/F = 1\text{ h}$, $\text{TOS} = 30\text{ min}$.

^a 2.5ReO_x refers to the monometallic 2.5Re catalyst without pretreatment at $450\text{ }^{\circ}\text{C}$ in H_2 for 1 h.

^b 5Ni+2.5Re refers to the physical mixture of 5Ni and 2.5Re.

^c Others include p-/o-cresol, cyclohexanone, cyclohexanol, and heavy products with carbon number higher than 8.

acid sites in zeolite [31], the weak acid sites in Ni–Re do not change the reaction pathway. Tests by feeding MCHol directly (see Table S1) produced very small amounts of dehydration products (methylcyclohexene, MCHene) as well as their hydrogenation products (methylcyclohexane, MCHane), but large amounts of dehydrogenation products (m-cresol and MCHone). Additional tests by feeding MCHone directly produced very little MCHene and MCHane (Table S1). These results indicate that complete hydrogenation of the aromatic ring of m-cresol to MCHol followed by dehydration to MCHene and further hydrogenation to MCHane or C–O hydrogenolysis to MCHane (HYD path) is not important over either catalyst.

Table 4 compares m-cresol conversion and product distributions over different type of catalysts at the same W/F of 0.5 h. The monometallic 2.5Re is much less active than 5Ni, while it is highly selective to Tol, and no hydrogenation or C–C hydrogenolysis products were detected. Interestingly, the 2.5Re sample without prerduction shows even lower activity. These results are consistent with Feng et al., who showed that Re has very low activity for HDO of 4-propylphenol [32], but in contrast to Leiva et al., who showed that Re is very active for HDO of guaiacol [61]. The differences may be results of very different reaction conditions (temperature, pressure, support, solvent). The catalytic performance of a physical mixture of 5Ni + 2.5Re appears to be the

sum of individual 5Ni and 2.5Re, indicating that Ni and Re work independently. However, compared with monometallic 5Ni, the conversion and the Tol yield improved by more than 4 and 10 times, respectively, on bimetallic 5Ni2.5Re. This improvement highlights the crucial role of Ni–Re neighboring sites working in synergy for high activity and selectivity toward toluene during HDO of m-cresol. Moreover, the promotional effect of Re on Ni is much greater than that of Fe on either Ni or Pd in the corresponding bimetallic catalysts [20,21].

The promotional role of Re was further studied by varying the amount of Re loading. The mass-based intrinsic reaction rate measured under differential reaction conditions is plotted in Fig. 12. The intrinsic reaction rate increases almost linearly from $0.536\text{ }\mu\text{mol g}_{\text{cat}}^{-1}\text{ s}^{-1}$ on 5Ni to 3.367 and $6.764\text{ }\mu\text{mol g}_{\text{cat}}^{-1}\text{ s}^{-1}$ on 5Ni2.5Re and 5Ni5Re, respectively. When the Re loading is further increased to 5Ni10Re, the intrinsic reaction rate only increases to $8.851\text{ }\mu\text{mol g}_{\text{cat}}^{-1}\text{ s}^{-1}$. The improvement factors are 6 and 12 for 5Ni2.5Re and 5Ni5Re, respectively. When the intrinsic reaction rate was normalized to moles of Re loading, the reaction rate was found to decrease when the Re loading was >5%.

The effect of the Re loading on the primary product distribution were investigated at m-cresol conversion of $\sim 11.5 \pm 1\%$, which was achieved by adjusting W/F (Fig. 13). Clearly, increasing the Re loading improved the direct deoxygenation to Tol, while it inhibited the

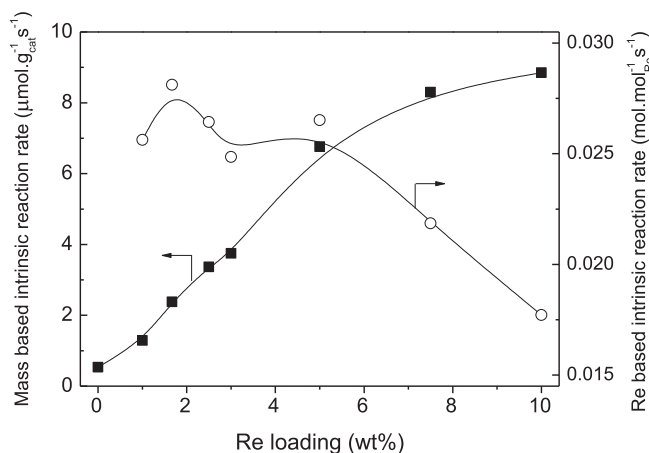


Fig. 12. Effect of Re loading on intrinsic reaction rate of m-cresol conversion based on mass of catalyst or moles of Re loading, measured under differential conditions with conversion <15%. Reaction conditions: $T = 300\text{ }^{\circ}\text{C}$, $P = 1\text{ atm}$, $\text{H}_2/\text{m-Cresol} = 60$, $\text{TOS} = 30\text{ min}$. W/F was varied to achieve m-cresol conversion <15%.

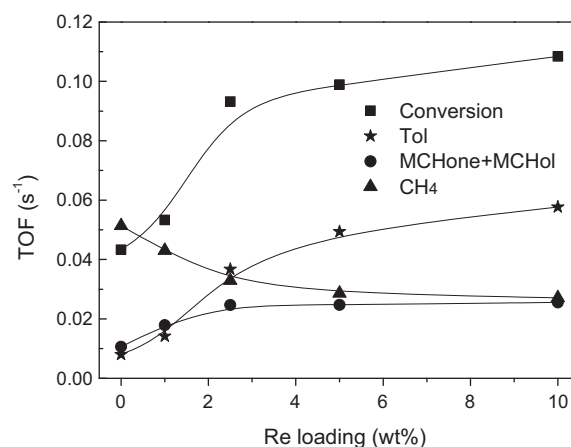


Fig. 14. Turnover frequencies of m-cresol conversion and production of toluene, methylcyclohexanone + methylcyclohexanol, and CH_4 . The reaction conditions are the same as in Fig. 12.

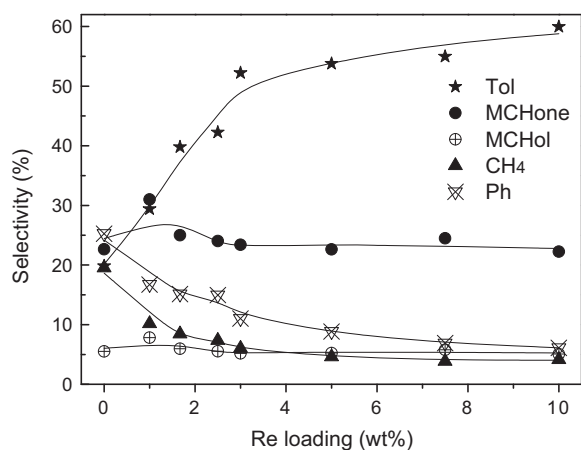


Fig. 13. Major products distribution as a function of Re loading at similar m-cresol conversion of $\sim 11.5 \pm 1\%$. The reaction conditions are the same as in Fig. 12.

C–C hydrogenolysis to CH_4 and Ph, with a slight reduction of the hydrogenation products (MCHone and MCHol). The effect of Re on the product distributions is more pronounced at Re loadings less than 3%.

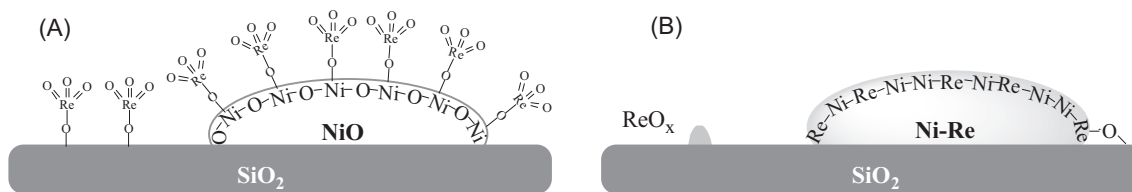
The mass-based intrinsic reaction rate may be influenced by both the number and the structure of the active sites. To distinguish these effects, the turnover frequencies (TOFs) of m-cresol conversion, deoxygenation to Tol, hydrogenation to MCHone and MCHol, and hydrogenolysis to CH_4 and Ph were calculated based on the number of active sites measured with CO chemisorption and plotted as a function of Re loading (Fig. 14). It should be noted that the stoichiometry of CO adsorption changes as a function of Re loading even though the CO/Ni ratio was assumed to be 1. However, this will not change the trend in Fig. 14. The TOF of m-cresol conversion doubled from 0.043 s^{-1} on 5Ni to 0.093 s^{-1} on 5Ni2.5Re, and then slowly increased to 0.108 s^{-1} on 5Ni10Re. A similar trend was observed for TOF of toluene formation, which increased more than four times from 0.008 s^{-1} on 5Ni to 0.037 s^{-1} on 5Ni2.5Re, and again slowly increased to 0.058 s^{-1} on 5Ni10Re. On the other hand, the TOF for MCHone + MCHol doubled from 0.011 s^{-1} on 5Ni to 0.025 s^{-1} on 5Ni2.5Re but only increased slightly to 0.026 s^{-1} on 5Ni10Re. In contrast, the TOF for CH_4 was almost halved from 0.052 s^{-1} on 5Ni to 0.033 s^{-1} on 5Ni2.5Re and further decreased

to 0.027 s^{-1} on 5Ni10Re. The results indicate that the increased number of active sites in bimetallic Ni–Re catalysts works synergistically with the structure of active sites to enhance the HDO activity and to improve the selectivity of deoxygenation to toluene.

3.4. Discussion

As shown in Scheme 2, the Re species in the fresh catalyst appears to be in the state of isolated ReO_4 species attaching to NiO particles or SiO_2 support. This Ni–Re interaction during calcination resulted in better dispersion of NiO on silica. Upon reduction, the Re atoms penetrate into the unit cell of Ni, forming intimate interactions, likely due to the similar d -spacing values of Ni(111) and Re(101). The Ni and Re form bulk Ni–Re alloys at Ni/Re ratios of 4/1 and 1/3, respectively [62], and their formation requires high temperatures. Consequently, reduction at $450\text{ }^{\circ}\text{C}$ may not lead to formation of bulk stoichiometric Ni–Re alloys, but formation of a nonstoichiometric surface Ni–Re alloy is likely, as shown by the enrichment of Re on the surface of Ni–Re particles (EDS and XPS results). The penetration of Re atoms into the surface layers of Ni particles will disrupt the continuity of Ni atoms and break the surface into smaller Ni ensembles, consequently changing the catalyst surface geometrically, as reflected in the increased L/B ratio of CO adsorption. In addition, the close proximity of Re and Ni also modifies the neighboring Ni atoms electronically, as indicated by the shifted core level of Ni to a higher BE in XPS and the blue shift of linearly adsorbed CO in FTIR. This is consistent with the previous work, which showed that Ni in bimetallic Ni–Re/CeO₂ and Ca-promoted Ni–Re catalysts become electron-deficient (cationic) due to the presence of Re in the vicinity, as evidenced by X-ray adsorption near-edge structure [50] and XPS [40]. In contrast to the Ni–Re catalysts, the electronic effect was absent in the bimetallic Ir–Re and Rh–Re catalysts [63,64]. This difference may be a result of a small Re ensemble only attached to the surfaces of Ir or Rh particles without penetration into their unit cells. Under those conditions, one would expect little electronic effect due to the limited interaction between Re and either Ir or Rh.

Several mechanisms have been proposed for selective direct deoxygenation of phenolics, including direct deoxygenation (DDO) [4], partial hydrogenation [65], and tautomerization [7,21]. In each mechanism, the C–O bond cleavage is the key step. On Group VIII metals, the cleavage of the C–O bond requires the adsorption of both C and O atoms on the two adjacent metal atoms [66–68]. On a monometallic Ni catalyst, phenol adsorbs on a bridge site through its phenyl ring with the O atom pointing away from



Scheme 2. Schematic representation of the structure of bimetallic Ni–Re catalyst before (A) and after (B) reduction at 450 °C for 1 h.

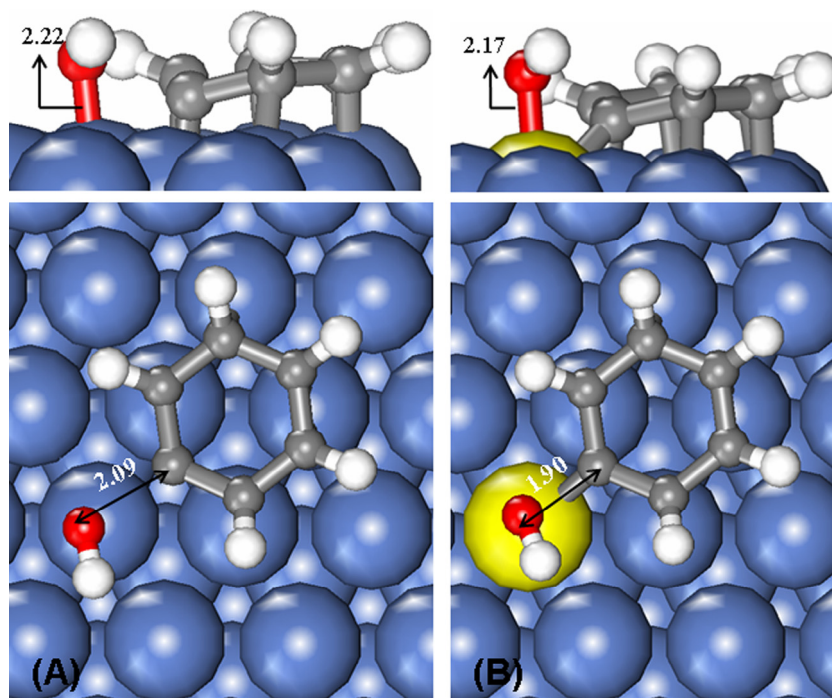


Fig. 15. Structure of the transition states of direct dehydroxylation of phenol on (A) Ni(111) surface and (B) (Re)Ni(111) surface. The unit of the numbers in the figure is Å.

the surface. To break the C–O bond, the adsorption of the O atom onto the surface Ni atom requires overcoming the strong repulsion between Ni and O, resulting in an increased activation barrier. Adding H atoms to the phenyl ring appears to occur more readily, since the ring is already on the surface. Therefore, hydrogenation of *m*-cresol to MCHone and MCHol is more favorable than deoxygenation of *m*-cresol to Tol at low conversions, particular when the reaction temperature is low [13]. On the other hand, when oxophilic Re is present in the surface of the bimetallic Ni–Re catalyst, both the phenyl ring and the O atom can adsorb onto the surface, with the phenyl ring on Ni with shortened C1–Ni bond and O on Re with lengthened C–O bond. The cleavage of the C–O bond occurs more readily, as the adsorption structure of phenolic on the Ni–Re surface alloy resembles the transition state where both C and O bound to the surface. Consequently, the TOF for deoxygenation of *m*-cresol to Tol increased by four times on 5Ni2.5Re from that on 5Ni. These results highlight the crucial role of the Ni–Re neighboring sites for the adsorption of the phenolics and the subsequent cleavage of the C–O bond. Similarly, one recent work suggested that the selective deoxygenation of phenol to benzene at the interface of Ru/TiO₂, where the O atom of phenol adsorbed in the oxygen vacancy or hydroxyl of TiO₂ and the phenyl ring adsorbed onto the Ru particle [69].

To demonstrate the importance of Ni–Re neighboring sites for the HDO reaction, we examined the direct dehydroxylation of phenol on both Ni(111) and (Re)Ni(111) surfaces. As shown in Fig. 10,

the reaction starts from the initial state, with the O atom of hydroxyl moving toward the nearest surface Ni or Re site, accompanied by elongation of the C1–O bond along the reaction coordinate. At the same time, C1 moves toward the hollow site and the phenyl ring rotates slightly. At the transition state on Ni(111), the distance of C1–O increases to 2.09 Å with OH adsorption on Ni (O–Ni distance of 2.22 Å) (Fig. 15A). In contrast, the transition state on the (Re)Ni(111) surface has a significantly shorter C1–O distance of 1.90 Å, attributable to a stronger O–Re interaction (O–Re distance of 2.17 Å) (Fig. 15B). In the final states (Fig. S4), the OH group moved further away from the phenyl ring to an adjacent Ni–Ni (C1–O distance 3.14 Å) or Ni–Re bridge site (C1–O distance 2.92 Å), with C1 in the hollow site. This elementary step is endothermic (reaction energy of 54.0 kJ/mol) with a high activation energy of 175.6 kJ/mol on Ni(111). In contrast, the same step becomes slightly exothermic (reaction energy of –5.8 kJ/mol) with a significantly reduced activation barrier of 94.6 kJ/mol on (Re)Ni(111). These results strongly indicate that the presence of the oxophilic Re next to Ni enhances the C–O cleavage by significantly reducing both the reaction energy and the activation barrier for direct deoxygenation, making this reaction pathway accessible, and even favorable under mild conditions.

Recent experimental and computational studies [7,14,70] suggest that HDO of *m*-cresol on Pt, particularly Pt supported on the reducible TiO₂ support, follows a tautomerization pathway to produce toluene. The current results do not allow us to exclude the

contribution of partial hydrogenation and tautomerization mechanisms to the apparent direct deoxygenation. In fact, the enhanced direct C–O cleavage (dehydroxylation) on the Ni–Re neighboring sites could also be an integral part of the C–O cleavage of the intermediate by a partial hydrogenation or tautomerization pathway to aromatics.

Even though Re plays an important role in adsorption of O atoms of phenolics and facilitates C–O cleavage, the activities of monometallic 2.5Re and 2.5ReO_x were rather low (Table 4). This may be due to the strong oxophilicity of Re, which leads to the accumulation of surface hydroxyl species from dehydroxylation, which eventually blocks the active sites for deoxygenation. When Ni is present next to Re, the surface hydroxyl on Re could be hydrogenated to H₂O on the Ni–Re neighboring sites by H atoms from Ni, resulting in the regeneration of active sites. Under working conditions, Ni–ReO_x with Re at a low degree of oxidation may also serve as an active site for deoxygenation.

Nickel catalysts have been shown to be highly active for hydrogenolysis of (cyclo)hydrocarbons directly to methane [71], and the reaction rate of hydrogenolysis of benzene increases with the Ni particle size [72], i.e., for large ensembles of close packed facets. Theoretical calculations suggest that the hydrogenolysis of C–C bonds requires complete dehydrogenation of two C atoms and formation of three C–Ni bonds for each C atom on two hollow sites prior to C–C cleavage [73,74]. That is, at least 4–6 neighboring Ni atoms (ensemble size 4–6) are required in the transition state for C–C cleavage. On monometallic 5Ni, large particles provide needed Ni ensembles for breaking the C–C bonds of ring and the successive hydrogenolysis of the terminal C–C bonds to form CH₄ [71]. On bimetallic Ni–Re, both TEM and FTIR of CO adsorption indicate that the proximity of Ni and Re breaks the Ni surface into small ensembles that do not favor the formation of the transition state, leading to the C–C bond breaking. Furthermore, the electronic effect would reduce the adsorption strength of deoxygenation products (Tol, Ben) on the surface, resulting in desorption of the products and preventing the subsequent degradation of the products through successive C–C hydrogenolysis. Consequently, the hydrogenolysis was greatly inhibited on the bimetallic catalyst.

The TOFs for hydrogenation of m-cresol to MCHone and MCHol were slightly increased (Fig. 14), while their selectivities were slightly reduced (Fig. 13). This might be a consequence of the strong promotional effect of Re for deoxygenation, making deoxygenation dominate hydrogenation, and resulting in slightly reduced selectivity toward hydrogenation.

We note that the promotional effect of Re is more pronounced at Re loadings of <5%. Re would interact directly with Ni at these low Re loadings. When Re loading is increased beyond 5%, additional Re may be isolated from Ni and disperse directly on silica. In the latter case, Re will have little promotional effect on Ni.

4. Conclusions

Monometallic 5%Ni/SiO₂ was unselective in catalyzing the primary reactions of deoxygenation to toluene, hydrogenation to 3-methylcyclohexanone and 3-methylcyclohexanol, and C–C hydrogenolysis to CH₄. Bimetallic 5%Ni–2.5%Re/SiO₂ improved the intrinsic reaction rate for hydrodeoxygenation of m-cresol by a factor of 6, and its TOF improved by a factor of 2. The bimetallic Ni–Re catalyst was highly selective for deoxygenation to toluene, with the TOF for deoxygenation increased by a factor of 4, while that for C–C hydrogenolysis is reduced to half.

The addition of Re to the Ni/SiO₂ catalyst stabilized the highly dispersed NiO through the strong Ni–O–Re interactions. Upon reduction, Re penetrated into the unit cell of Ni, forming surface Ni–Re alloy. The bimetallic catalysts exhibit both geometric and

electronic effects: (1) Re breaks the Ni surface into small ensembles and provides Ni–Re neighboring sites, and (2) the proximity between Ni and Re reduce the Ni *d*-band occupancy. In contrast to phenol adsorption on the bare Ni(111) surface through the phenyl ring with O pointing away from the surface, the adsorption of phenol on (Re)Ni(111) through the phenyl ring on Ni and O on Re on the Ni–Re neighboring sites facilitates C–O bond cleavage. The Ni ensembles with a reduced size inhibit the formation of the structure that is favored by the transition state of C–C hydrogenolysis. In addition, electron deficiency in the Ni *d* band weakens the adsorption of phenyl rings on the surface and therefore prevents the C–C hydrogenolysis of aromatic products.

Acknowledgments

The authors thank the National Natural Science Foundation of China (21676194 and 21373148) and the Ministry of Education of China for the Program of New Century Excellent Talents in University (NCET-12-0407) for their support.

Appendix A. Supplementary material

Supplementary data associated with this article can be found, in the online version, at <http://dx.doi.org/10.1016/j.jcat.2017.01.001>.

References

- [1] J. Zakzeski, P.C.A. Bruijninx, A.L. Jongorius, B.M. Weckhuysen, The catalytic valorization of lignin for the production of renewable chemicals, *Chem. Rev.* 110 (2010) 3552–3599.
- [2] M. Saidi, F. Samimi, D. Karimipourfar, T. Nimmanwudipong, B.C. Gates, M.R. Rahimpour, Upgrading of lignin-derived bio-oils by catalytic hydrodeoxygenation, *Energy Environ. Sci.* 7 (2014) 103–129.
- [3] X. Zhu, L.L. Lobban, R.G. Mallinson, D.E. Resasco, Bifunctional transalkylation and hydrodeoxygenation of anisole over a Pt/HBeta catalyst, *J. Catal.* 281 (2011) 21–29.
- [4] H. Weigold, Behaviour of Co–Mo–Al₂O₃ catalysts in the hydrodeoxygenation of phenols, *Fuel* 61 (1982) 1021–1026.
- [5] Y. Romero, F. Richard, S. Brunet, Hydrodeoxygenation of 2-ethylphenol as a model compound of bio-crude over sulfided Mo-based catalysts: Promoting effect and reaction mechanism, *Appl. Catal. B* 98 (2010) 213–223.
- [6] E.J. Shin, M.A. Keane, Gas-phase hydrogenation/hydrogenolysis of phenol over supported nickel catalysts, *Ind. Eng. Chem. Res.* 39 (2010) 883–892.
- [7] L. Nie, D.E. Resasco, Kinetics and mechanism of m-cresol hydrodeoxygenation on a Pt/SiO₂ catalyst, *J. Catal.* 317 (2014) 22–29.
- [8] X. Zhu, R.G. Mallinson, D.E. Resasco, Role of transalkylation reactions in the conversion of anisole over HZSM-5, *Appl. Catal. A* 379 (2010) 172–181.
- [9] M. Shetty, K. Murugappan, T. Prasomsri, W.H. Green, Y.R. Leshkov, Reactivity and stability investigation of supported molybdenum oxide catalysts for the hydrodeoxygenation (HDO) of m-cresol, *J. Catal.* 331 (2015) 86–97.
- [10] J.S. Moon, E.G. Kim, Y.K. Lee, Active sites of Ni₂P/SiO₂ catalyst for hydrodeoxygenation of guaiacol: A joint XAFS and DFT study, *J. Catal.* 311 (2014) 144–152.
- [11] W.S. Lee, Z. Wang, R.J. Wu, A. Bhan, Selective vapor-phase hydrodeoxygenation of anisole to benzene on molybdenum carbide catalysts, *J. Catal.* 319 (2014) 44–53.
- [12] R. Olcese, M.M. Bettahar, B. Malaman, J. Ghanbaja, L. Tibavizco, D. Petitjean, A. Dufour, Gas-phase hydrodeoxygenation of guaiacol over iron-based catalysts. Effect of gases composition, iron load and supports (silica and activated carbon), *Appl. Catal. B* 129 (2013) 528–538.
- [13] C. Chen, G. Chen, F. Yang, H. Wang, J. Han, Q. Ge, X. Zhu, Vapor phase hydrodeoxygenation and hydrogenation of m-cresol on silica supported Ni, Pd and Pt catalysts, *Chem. Eng. Sci.* 135 (2015) 145–154.
- [14] Q. Tan, G. Wang, L. Nie, A. Dinse, C. Buda, J. Shabaker, D.E. Resasco, Different product distributions and mechanistic aspects of the hydrodeoxygenation of m-Cresol over platinum and ruthenium catalysts, *ACS Catal.* 5 (2015) 6271–6283.
- [15] E.J. Shin, M.A. Keane, Catalytic hydrogen treatment of aromatic alcohols, *J. Catal.* 173 (1996) 450–459.
- [16] T.M. Huynh, U. Armbruster, M.M. Pohl, M. Schneider, J. Radnik, D.L. Hoang, B. M.Q. Phan, D.A. Nguyen, A. Martin, Hydrodeoxygenation of phenol as a model compound for bio-oil on non-noble bimetallic nickel-based catalysts, *ChemCatChem* 6 (2014) 1940–1951.
- [17] A. Robinson, G.A. Ferguson, J.R. Gallagher, S. Cheah, G.T. Beckham, J.A. Schaidle, J.E. Hensley, J.W. Medlin, Enhanced hydrodeoxygenation of m-Cresol over bimetallic Pt–Mo catalysts through an oxophilic metal-induced tautomerization pathway, *ACS Catal.* 6 (2016) 4356–4368.

- [18] P.T.M. Do, A.J. Foster, J.G. Chen, R.F. Lobo, Bimetallic effects in the hydrodeoxygenation of meta-cresol on γ -Al₂O₃ supported Pt–Ni and Pt–Co catalysts, *Green Chem.* 14 (2012) 1388–1397.
- [19] D. Shi, L.A. Ramirez, J.M. Vohs, The use of bimetallics to control the selectivity for the upgrading of lignin-derived oxygenates: Reaction of anisole on Pt and PtZn catalysts, *J. Catal.* 340 (2016) 219–226.
- [20] J. Sun, A.M. Karim, H. Zhang, L. Kovarik, X.S. Li, A.J. Hensley, J.S. McEwen, Y. Wang, Carbon-supported bimetallic Pd–Fe catalysts for vapor-phase hydrodeoxygenation of guaiacol, *J. Catal.* 306 (2013) 47–57.
- [21] L. Nie, P.M. de Souza, F.B. Noronha, W. An, T. Sooknoi, D.E. Resasco, Selective conversion of m-cresol to toluene over bimetallic Ni–Fe catalysts, *J. Mol. Catal. A* 388–389 (2014) 47–55.
- [22] Y. Hong, H. Zhang, J. Sun, K.M. Ayman, A.J.R. Hensley, M. Gu, M.H. Engelhard, J. S. McEwen, Y. Wang, Synergistic catalysis between Pd and Fe in gas phase hydrodeoxygenation of m-Cresol, *ACS Catal.* 4 (2014) 3335–3345.
- [23] S. Ted Oyama, T. Onkawa, A. Takagaki, R. Kikuchi, S. Hosokai, Y. Suzuki, K.K. Bando, Production of phenol and cresol from guaiacol on nickel phosphide catalysts supported on acidic supports, *Top. Catal.* 58 (2015) 201–210.
- [24] X. Zhu, L. Nie, L.L. Lobban, R.G. Mallinson, D.E. Resasco, Efficient conversion of m-Cresol to aromatics on a bifunctional Pt/HBeta catalyst, *Energy Fuels* 28 (2014) 4104–4111.
- [25] G. Kresse, J. Furthmüller, Efficiency of ab-initio total energy calculations for metals and semiconductors using a plane-wave basis set, *Phys. Rev. B Condens. Matter* 47 (1993) 558–561.
- [26] G. Kresse, J. Furthmüller, Efficiency of ab-initio total energy calculations for metals and semiconductors using a plane-wave basis, *Comput. Mater. Sci.* 6 (1996) 15–50.
- [27] G. Kresse, Efficient iterative schemes for ab initio total-energy calculation using a plane-wave basis set, *Phys. Rev. B* 54 (1996) 11169–11186.
- [28] P.E. Blöchl, Projector augmented-wave method, *Phys. Rev. B* 50 (1994) 17953–17979.
- [29] J.P. Perdew, K. Burke, M. Ernzerhof, Generalized gradient approximation made simple, *Phys. Rev. Lett.* 77 (1996) 3865–3868.
- [30] G. Li, J. Han, H. Wang, X. Zhu, Q. Ge, Role of dissociation of phenol in its selective hydrogenation on Pt(111) and Pd(111), *ACS Catal.* 5 (2015) 2009–2016.
- [31] Q. Sun, G. Chen, H. Wang, X. Liu, J. Han, Q. Ge, X. Zhu, Insights into the major reaction pathways of vapor-phase hydrodeoxygenation of m-Cresol on a Pt/HBeta catalyst, *ChemCatChem* 8 (2016) 551–561.
- [32] B. Feng, H. Kobayashi, H. Ohta, A. Fukuoka, Aqueous-phase hydrodeoxygenation of 4-propylphenol as a lignin model to n-propylbenzene over Re–Ni/ZrO₂ catalysts, *J. Mol. Catal. A* 388–389 (2014) 41–46.
- [33] L. Wang, K. Murata, Y. Matsumura, M. Inaba, Lower-temperature catalytic performance of bimetallic Ni–Re/Al₂O₃ catalyst for gasoline reforming to produce hydrogen with the inhibition of methan formation, *Energy Fuels* 20 (2006) 1377–1381.
- [34] S. Sittitha, W. An, D.E. Resasco, Selective conversion of furfural to methylfuran over silica-supported Ni–Fe bimetallic catalysts, *J. Catal.* 284 (2011) 90–101.
- [35] E.L. Lee, I.E. Wachs, In situ spectroscopic investigation of the molecular and electronic structures of SiO₂ supported surface metal oxides, *J. Phys. Chem. C* 111 (2007) 14410–14425.
- [36] A. Aminzadeh, H.S. Fard, Raman spectroscopic study of Ni/Al₂O₃ catalyst, *Spectrochim. Acta A* 55 (1999) 1421–1425.
- [37] D.S. Kim, I.E. Wachs, Surface rhenium oxide–support interaction for supported Re₂O₇ catalysts, *J. Catal.* 141 (1993) 419–429.
- [38] M.A. Vuurman, D.J. Stufkens, A. Oskam, Structural determination of surface rhenium oxide on various oxide supports (Al₂O₃, ZrO₂, TiO₂ and SiO₂), *J. Mol. Catal. A* 76 (1992) 263–285.
- [39] Y. Amada, H. Watanabe, M. Tamura, Y. Nakagawa, K. Okumura, K. Tomishige, Structure of ReO_x clusters attached on the Ir metal surface in Ir–ReO_x/SiO₂ for the hydrogenolysis reaction, *J. Phys. Chem. C* 116 (2012) 23503–23514.
- [40] S. Engels, J. Eick, W. Morke, U. Maier, I. Boszormenyi, K. Matusek, Z. Schay, L. Gucci, Characterization and catalytic activity of unsupported nickel–rhenium catalysts modified by calcium oxide, *J. Catal.* 103 (1987) 105–114.
- [41] G. Beamson, A.J. Papworth, C. Philipps, A.M. Smith, R. Whyman, Selective hydrogenation of amides using bimetallic Ru/Re and Rh/Re catalysts, *J. Catal.* 278 (2011) 228–238.
- [42] J.A. Rodriguez, Physical and chemical properties of bimetallic surfaces, *Surf. Sci. Rep.* 24 (1996) 223–287.
- [43] S. Sittitha, T. Pham, T. Prasomsri, T. Sooknoi, R.G. Mallinson, D.E. Resasco, Conversion of furfural and 2-methylpentanal on Pd/SiO₂ and Pd–Cu/SiO₂ catalysts, *J. Catal.* 280 (2011) 17–27.
- [44] X. Zhu, Y. Zhang, C. Liu, CO adsorbed infrared spectroscopy study of Ni/Al₂O₃ catalyst for CO₂ reforming of methane, *Catal. Lett.* 118 (2007) 306–312.
- [45] D.G. Blackmond, E.I. Ko, Structural sensitivity of CO adsorption and H₂ CO coadsorption on NiSiO₂ catalysts, *J. Catal.* 96 (1985) 210–221.
- [46] M.S. Nacheff, L.S. Kraus, M. Ichikawa, B.M. Hoffman, J.B. Butt, W.M.H. Sachtler, Characterization and catalytic function of Re⁰ and Re⁴⁺ in Re/Al₂O₃ and Pt/Re/Al₂O₃ catalysts, *J. Catal.* 106 (1987) 263–272.
- [47] E.L. Kunkes, D.A. Simonetti, J.A. Dumesic, W.D. Pyrz, L.E. Murillo, J.G. Chen, D.J. Buttrey, The role of rhenium in the conversion of glycerol to synthesis gas over carbon supported platinum–rhenium catalysts, *J. Catal.* 260 (2008) 164–177.
- [48] J.A. Anderson, F.K. Chong, C.H. Rochester, IR study of CO adsorption on Pt, Re and Pt–Re/Al₂O₃ catalysts before and after coking, *J. Mol. Catal. A* 140 (1999) 65–80.
- [49] Y. Sato, Y. Soma, T. Miyao, S. Naito, The water–gas–shift reaction over Ir/TiO₂ and Ir–Re/TiO₂ catalysts, *Appl. Catal. A* 304 (2006) 78–85.
- [50] K. Chayakul, T. Srihanratana, S. Hengrasmee, Catalytic activities of Re–Ni/CeO₂ bimetallic catalysts for water gas shift reaction, *Catal. Today* 175 (2011) 420–429.
- [51] C. Zhao, S. Kasakov, J. He, J.A. Lercher, Comparison of kinetics, activity and stability of Ni/HZSM-5 and Ni/Al₂O₃–HZSM-5 for phenol hydrodeoxygenation, *J. Catal.* 296 (2012) 12–23.
- [52] X. Zhu, L.L. Lobban, R.G. Mallinson, D.E. Resasco, Tailoring the mesopore structure of HZSM-5 to control product distribution in the conversion of propanal, *J. Catal.* 271 (2010) 88–98.
- [53] T.J.G. Kofke, R.J. Gorte, G.T. Kokotailo, W.E. Farneth, Stoichiometric adsorption complexes in H-ZSM-5, H-ZSM-12, and H-mordenite zeolites, *J. Catal.* 115 (1989) 265–272.
- [54] K.M. Jiang, T. Kawai, T. Ishikawa, FT-IR and TPD studies of adsorbed pyridine on Re₂O₇–Al₂O₃ catalysts, *J. Catal.* 159 (1996) 288–295.
- [55] D. Hibbitts, Q. Tan, M. Neurock, Acid strength and bifunctional catalytic behavior of alloys comprised of noble metals and oxophilic metal promoters, *J. Catal.* 315 (2014) 48–58.
- [56] L.D. Site, A. Alavi, C.F. Abrams, Adsorption energies and geometries of phenol on the (111) surface of nickel: An ab initio study, *Phys. Rev. B* 67 (2003).
- [57] M.L. Honkela, J. Björk, M. Persson, Computational study of the adsorption and dissociation of phenol on Pt and Rh surfaces, *Phys. Chem. Chem. Phys.* 14 (2012) 5849–5854.
- [58] Y. Yoon, R. Rousseau, R.S. Weber, D. Mei, J.A. Lercher, First-principles study of phenol hydrogenation on Pt and Ni catalysts in aqueous phase, *J. Am. Chem. Soc.* 136 (2014) 10287–10298.
- [59] H. Ihm, J.M. White, Stepwise dissociation of thermally activated phenol on Pt (111), *J. Phys. Chem. B* 104 (2000) 6202–6211.
- [60] A.J.R. Hensley, Y. Wang, J.S. McEwen, Adsorption of phenol on Fe (110) and Pd (111) from first principles, *Surf. Sci.* 630 (2014) 244–253.
- [61] K. Leiva, N. Martinez, C. Sepulveda, R. Garcia, C.A. Jiménez, D. Laurenti, M. Vrinat, C. Geantet, J.L.G. Fierro, I.T. Ghampson, N. Escalona, Hydrodeoxygenation of 2-methoxyphenol over different Re active phases supported on SiO₂ catalysts, *Appl. Catal. A* 490 (2015) 71–79.
- [62] O. Levy, M. Jahnátek, R.V. Chepulsii, G.L.W. Hart, S. Curtarolo, Ordered structure in rhenium binary alloys from first-principles calculations, *J. Am. Chem. Soc.* 133 (2010) 158–162.
- [63] Y. Amada, Y. Shinmi, S. Koso, T. Kubota, Y. Nakagawa, K. Tomishige, Reaction mechanism of the glycerol hydrogenolysis to 1,3-propanediol over Ir–ReO_x/SiO₂ catalyst, *Appl. Catal. B* 105 (2011) 117–127.
- [64] M. Chia, Y.J.P. Torres, D. Hibbitts, Q. Tan, H.N. Pham, A.K. Datye, M. Neurock, R.J. Davis, J.A. Dumesic, Selective hydrogenolysis of polyols and cyclic ethers over bifunctional surface sites on rhodium–rhenium catalysts, *J. Am. Chem. Soc.* 133 (2011) 12675–12689.
- [65] F.E. Massoth, P. Politzer, M.C. Concha, J.S. Murray, J. Jakowski, J. Simons, Catalytic hydrodeoxygenation of methyl-substituted phenols: correlations of kinetic parameters with molecular properties, *J. Phys. Chem. B* 110 (2006) 14283–14291.
- [66] G.H. Gu, C.A. Mullen, A.A. Boateng, D.G. Vlachos, Mechanism of dehydration of phenols on noble metals via first-principles microkinetic modeling, *ACS Catal.* 6 (2016) 3047–3055.
- [67] C. Chiu, A. Genest, A. Borgna, N. Rösch, Hydrodeoxygenation of guaiacol over Ru(0001): A DFT Study, *ACS Catal.* 4 (2014) 4178–4188.
- [68] J. Lu, A. Heyden, Theoretical investigation of the reaction mechanism of the hydrodeoxygenation of guaiacol over a Ru(0001) model surface, *J. Catal.* 321 (2015) 39–50.
- [69] R.C. Nelson, B. Baek, P. Ruiz, B. Goundie, A. Brooks, M.C. Wheeler, B.G. Frederick, L.C. Grabow, R.N. Austin, Experimental and theoretical insights into the hydrogen-efficient direct hydrodeoxygenation mechanism of phenol over Ru/TiO₂, *ACS Catal.* 5 (2015) 6509–6523.
- [70] M.B. Griffin, G.A. Ferguson, D.A. Ruddy, M.J. Biddy, G.T. Beckham, J.A. Schaidle, Role of the support and reaction conditions on the vapor-phase deoxygenation of m-cresol over Pt/C and Pt/TiO₂ catalysts, *ACS Catal.* 6 (2016) 2715–2727.
- [71] G. Leclercq, S. Pietrzyk, M. Peyrovi, M. Karroua, Hydrogenolysis of saturated hydrocarbons: V. Influence of hydrocarbon structures on the activity and selectivity of Ni on silica, *J. Catal.* 99 (1986) 1–11.
- [72] P.H. Desai, J.T. Richardson, Crystallite size effects in Nickel catalysts: cyclohexane dehydrogenation and hydrogenolysis, *J. Catal.* 98 (1986) 392–400.
- [73] D.D. Hibbitts, D.W. Flaherty, E. Iglesia, Role of branching on the rate and mechanism of C–C cleavage in alkanes on metal surfaces, *ACS Catal.* 6 (2016) 469–482.
- [74] Z. Zhao, L.V. Moskaleva, N. Rösch, Tuning the selectivity for ring-opening reactions of methylcyclopentane over Pt catalysts: A mechanistic study from first-principles calculations, *J. Catal.* 285 (2012) 124–133.